PAPER

Check for updates

Effective electrochemical water oxidation to H$_2$O$_2$ based on a bimetallic Fe/Co metal–organic framework

Kunpeng Liu,†[ab] Xu Wang,†[ab] Nan Wang,*[ac] Ruiyong Zhang, [ID] *[ac] Meinan Yang,[a] Baorong Hou[ac] and Wolfgang Sand[a]

Rationally designing high-efficiency catalysts for electrochemical two-electron water oxidation reaction (2e$^-$ WOR) to produce hydrogen peroxide (H$_2$O$_2$) is extremely important, while designing bimetallic metal–organic frameworks (MOFs) is of great significance for effective 2e$^-$ WOR. Herein, MIL-53(Fe) and different proportions of Co-doped MIL-53(Fe) were prepared by a hydrothermal method. The structural characterization and elemental analysis showed that the Co ions were successfully doped into MIL-53(Fe) to form a MIL-53(Fe/Co) bimetallic MOF, and the morphology of MIL-53(Fe/Co) became more regular after Co doping. We found that the optimized MIL-53(Fe/Co) exhibits remarkable 2e$^-$ WOR performance, which gave an overpotential of 150 mV at 1 mA cm^{-2}. The overpotential of MIL-53(Fe/Co) was approximately 220 mV (at 1 mA cm^{-2}) lower than that of MIL-53(Fe), which may be attributed to the change of microstructure of MIL-53(Fe) after Co doping and the synergistic effect between Fe/Co. Our work introduces a strategy for designing bimetallic MOF-based electrocatalysts, opening up new possibilities for efficient 2e$^-$ WOR systems.
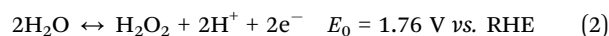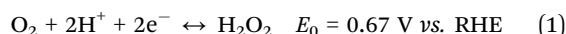
1. Introduction

Hydrogen peroxide is an environmentally friendly oxidizing agent. In addition to the anthraquinone method, which is a main technique for H$_2$O$_2$ synthesis at present,[1,2] electrochemical H$_2$O$_2$ preparation has attracted extensive attention. This method has the advantages of environmental friendliness, less by-products, *in situ* synthesis, and not requiring additional gas supply.[3–5] There are two methods for electrosynthesis of H$_2$O$_2$: the two-electron oxygen reduction reaction (2e$^-$ ORR, eqn (1)) and the two-electron water oxidation reaction (eqn (2)).[6] H$_2$O$_2$ synthesis *via* the 2e$^-$ ORR has been extensively researched in recent years,[7,8] and it has reached a high value of H$_2$O$_2$ production rate and Faraday efficiency (FE).[9,10] However, the drawbacks of this approach are that it requires a constant supply of oxygen gas. Compared to the 2e$^-$ ORR, the WOR requires no additional aeration. The process is simple and has more practical application prospects.[11]

$$O_2 + 2H^+ + 2e^- \leftrightarrow H_2O_2 \quad E_0 = 0.67 \text{ V } vs. \text{ RHE} \quad (1)$$

$$2H_2O \leftrightarrow H_2O_2 + 2H^+ + 2e^- \quad E_0 = 1.76 \text{ V } vs. \text{ RHE} \quad (2)$$

Generally, a suitable anode material for the 2e$^-$ WOR should have some prerequisite properties, including high stability to fulfil the demand for long-term operation, high selectivity to prevent the formation of by-products and high activity to save energy input.[12] At present, a variety of metal oxides have been developed for H$_2$O$_2$ generation *via* the 2e$^-$ WOR owing to their high selectivity and excellent stability under oxidation conditions, such as ZnO,[13] WO$_3$,[14] SnO$_2$,[15] TiO$_2$,[16] BiVO$_4$[17] and CaSnO$_3$.[18] However, due to the poor conductivity of metal oxides, these electrocatalysts generally show relatively low current density, which leads to low H$_2$O$_2$ yield.[19] Carbon materials generally possess relatively high electrical conductivity and electrochemical stability, for instance, carbon cloth (CC), carbon felt (CF), carbon-based materials boron-doped diamond (BDD) and PTFE modified carbon fiber paper (CFP).[20–22] But the low selectivity limits the application of carbon materials. As a consequence, high selectivity and high H$_2$O$_2$ production yield are hardly achieved simultaneously.

Transition metal–organic frameworks have gained considerable attention in recent years due to their large specific surface area, more active sites and large porosity.[23,24] Significantly, the inherent flexibility of MOFs has empowered researchers to fabricate a diverse array of MOF-based materials possessing distinct structures and functionalities.[25] Currently, iron-based

[a] Key Laboratory of Advanced Marine Materials, Key Laboratory of Marine Environmental Corrosion and Bio-fouling, Institute of Oceanology, Chinese Academy of Sciences, Qingdao, 266071, China. E-mail: wangnan123@qdio.ac.cn, ruiyong.zhang@qdio.ac.cn

[b] College of Materials Science and Engineering, Qingdao University of Science and Technology, 53 Zhengzhou Rd., Qingdao, Shandong 266042, China

[c] Institute of Marine Corrosion Protection, Guangxi Academy of Sciences, Nanning 530007, P. R. China

† These authors contributed to the work equally and should be regarded as co-first authors.

MOFs have broad development prospects and excellent research value.[26] However, their electrocatalytic performances are far from meeting the needs of practical applications due to their instability, poor electrical conductivity, and solvent-free or water-solvent conditions.[27,28] To overcome these limitations, extensive research endeavors have been devoted to exploring multiple approaches. An effective method is to hybridize the MOF with secondary highly conductive carriers, such as graphene and polyaniline.[29] However, using this method may block the micropores of the MOF, which would severely limit the effective mass transfer during electrocatalysis.[30]

Another method is to use a MOF as a precursor to prepare high performance electrocatalysts such as metal oxides, porous carbon and metal sulfides at high temperature,[31,32] but it may destroy the ordered channel structure of the MOF and sacrifice the metal active sites.[33,34] In recent years, novel composite materials with bimetallic MOFs have gained considerable attention in heterogeneous catalysis.[35] This approach preserves the MOF's skeleton while enhancing cycling stability and interfacial electron transfer efficiency.[36] Bimetallic MOF-based composites have many advantages over monometallic MOF-based materials: (i) different monometallic MOFs have different metallic elements, organic ligands, morphology, and structure, which can be prepared by different combination strategies to construct bimetallic MOF materials with different compositions, structures, and functions; (ii) most monometallic MOFs have undeveloped holes, but the synthesis of binary metal MOFs can further effectively improve this property. In addition, the preparation process of bimetallic MOFs is relatively simple and mild; (iii) the regular staggered arrangement of metal ions (or metal ion clusters) and organic ligands in bimetallic MOF structures is conducive to further fixing and dispersing metals (or metal oxides), improving the stability and catalytic activity of materials.[37] While the development of bimetallic MOFs is still in its infancy, an increasing number of studies demonstrate their great potential in various practical applications.[38]

Motivated by these concepts, we prepared MIL-53(Fe/Co) for electrocatalytic synthesis of H_2O_2 by a hydrothermal method and carried out structural characterization and elemental analysis, which manifest that the introduction of Co atoms precisely replaces the Fe site in MIL-53(Fe) to form MIL-53(Fe/Co) bimetallic MOF. Meanwhile we investigated the electrocatalytic WOR performance of MIL-53(Fe) and MIL-53(Fe/Co). Compared with MIL-53(Fe), MIL-53(Fe/Co) exhibits improved WOR activity. The results showed that the MIL-53(Fe/Co) bimetallic MOF showed good synergistic catalysis.

2. Experimental section

2.1. Materials

N,N-Dimethylformamide (DMF) was purchased from Macklin Biochemical Co., Ltd (Shanghai, China). Ferric chloride hexahydrate (FeCl$_3$·6H$_2$O), cobalt(ii) acetate tetrahydrate ((CH$_3$COO)$_2$Co·4H$_2$O), potassium hydrogen carbonate (KHCO$_3$), methanol and ethyl alcohol were purchased from Macklin Biochemical Co.,

Ltd (Shanghai, China). Cerium(iv) sulfate tetrahydrate (Ce(SO$_4$)$_2$) and isopropyl alcohol were purchased from Shanghai Aladdin Bio-Chem Technology Co., Ltd. Terephthalic acid was purchased from Tianjin Guangfu Fine Chemical Research Institute (Tianjin, China). Disodium terephthalate was purchased from Sinopharm Chemical Reagent Co., Ltd (China). 2,3-Bis(2methoxy-4-nitro-5-sulfophehyl)-2H-tetrazolium-5-carboxanilide (XTT) was purchased from Yuanye Co., Ltd, China. All experimental reagents and chemicals were used without further purification.

2.2. Material preparation

2.2.1. MIL-53(Fe). In a typical experiment,[39] FeCl$_3$·6H$_2$O (6 mmol) and terephthalic acid (6 mmol) were added to 30 mL of DMF solution. After ultrasonication for about 15 min, the mixture was transferred to a Teflon-lined stainless-steel autoclave with a volume capacity of 50 mL and heated at 150 °C for 12 h. After heat treatment, the autoclave was allowed to cool naturally to room temperature, and the products were collected by centrifugation at 7000 rpm for five minutes. To remove the solvent, the obtained powder was washed with ethyl alcohol and deionized water 3 times, respectively, and dried at 60 °C for 12 h under vacuum to obtain the MIL-53(Fe) catalyst.

2.2.2. MIL-53(Fe/Co). FeCl$_3$·6H$_2$O (1.2 mmol), (CH$_3$COO)$_2$-Co·4H$_2$O (4.8 mmol) and terephthalic acid (6 mmol) were added to 30 mL of DMF solution. After ultrasonication for about 15 min, the mixture was transferred to a Teflon-lined stainless-steel autoclave with a volume capacity of 50 mL and heated at 150 °C for 12 h. After heat treatment, the autoclave was allowed to cool naturally to room temperature, and the products were collected by centrifugation at 7000 rpm for five minutes. To remove the solvent, the obtained powder was washed with ethyl alcohol and deionized water 3 times, respectively, and dried at 60 °C sustained for 12 h under vacuum to obtain the MIL-53(Fe : Co = 1 : 4) catalyst. By varying the proportion of FeCl$_3$·6H$_2$O to (CH$_3$COO)$_2$Co·4H$_2$O, we successfully synthesized MIL-53(Fe), MIL-53(Fe : Co = 4 : 1), MIL-53(Fe : Co = 3 : 2) and MIL-53(Fe : Co = 2 : 3), and when the FeCl$_3$·6H$_2$O content is zero, we synthesized a purple sample called MIL-53(Co).

2.3. Characterization

The crystal structure and micromorphology of the samples were analyzed using an X-ray diffractometer (XRD, Rigaku, Japan) and scanning electron microscope (SEM, HITCH, Japan), respectively. The chemical state of the samples was measured by X-ray photoelectron spectroscopy (XPS, ESCALAB 250Xi, Thermo Fisher Scientific, USA). The oxygen vacancies of the samples were measured by electron paramagnetic resonance (EPR, Bruker-E500, Germany). The photoelectrochemical properties of the samples were tested on the standard three-electrode system of the CHI 660E electrochemical workstation (Shanghai Chenhua Instrument Co, China). UV-vis absorption spectra were acquired using a UV-vis spectrophotometer (UV-vis, HITCH 3900, Japan).

2.4. Electrochemical measurements

The electrochemical (EC) measurements were conducted in a three-electrode system, where a saturated calomel electrode

(SCE) and graphite were used as the reference and counter electrodes, respectively. The catalyst-coated fluorine-doped tin oxide (FTO) was used as the working electrode and the test area is 0.2826 cm^2. Dispersions with 5 mg of catalysts were prepared in 1 mL of isopropyl alcohol and homogenized in an ultrasonic bath for 20 min. 5 μL Nafion solution was then added into above the catalyst solution and homogenized in an ultrasonic bath for 20 min again. After homogenization, 10 μL of the solution was placed in the working electrode and dried.

The electrolyte solution is 2.0 M KHCO$_3$. Linear sweep voltammetry (LSV) was conducted in the potential range of 1.5–2.75 V (*vs.* RHE) at a scan rate of 10 mV s^{-1}. The conditions for measuring electrochemical impedance spectroscopy (EIS) were 0.05 V amplitude and 100 kHz–0.01 Hz frequency.

2.5. Detection of H$_2$O$_2$ production

Electrocatalytic H$_2$O$_2$ production on FTO loaded with catalysts was performed in a two-compartment cell with Nafion 117 membrane as a separator. Both the cathode compartment (30 mL) and anode compartment were filled with the same electrolyte (2.0 M KHCO$_3$).

The H$_2$O$_2$ concentration was measured by a traditional cerium sulfate Ce(SO$_4$)$_2$ titration method based on the mechanism that a yellow solution of Ce^{4+} would be reduced by H$_2$O$_2$ to colorless Ce^{3+} (eqn (3)).[40] Thus, the concentration of Ce^{4+} before and after the reaction can be measured by ultraviolet-visible spectroscopy. The wavelength used for the measurement was 316 nm.

$$2Ce^{4+} + H_2O_2 \rightarrow 2Ce^{3+} + 2H^+ + O_2 \qquad (3)$$
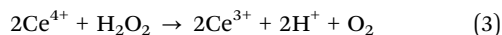
Therefore, the concentration of H$_2$O$_2$ (*M*) can be determined by eqn (4) where $M_{Ce^{4+}}$ is the mole of consumed Ce^{4+}.

$$M = 2 \times M_{Ce^{4+}} \qquad (4)$$

3. Results and discussion

3.1. Characterizations

According to Fig. 1, the synthesis of MIL-53(Fe/Co) was achieved through a one-step hydrothermal method. Subsequently, SEM images were collected to characterize the microstructure of the precursor and the composite. As seen from Fig. 2a, the images show that the MIL-53(Fe) displayed rod-like crystallites with a rough surface with diameters of ∼0.5 μm. With the incorporation of Co^{2+}, the surface morphology of MIL-53(Fe) was changed obviously. As shown in Fig. 2b–e, MIL-53(Fe/Co) displayed a typical bipyramidal prism structure with sharp edges and had a smooth surface, indicating that Co ion doping can regulate the MOF morphology of MIL-53(Fe). And the SEM images showed that the MIL-53(Fe/Co) with different proportions had different sizes. With the increase in the Co^{2+} percentage from 20 to 80% in the MIL-53(Fe/Co), the bipyramidal morphology of MIL-53(Fe/Co) gradually became smaller and the prism of MIL-53(Fe/Co) gradually became longer. However, the MIL-53(Co) showed a random block when only single-metal Co is present (Fig. 2f). This may be due to the fact that after Co ions are completely doped to replace Fe ions, the destruction of the original ordered structure of MIL-53(Fe) weakens the connection between metal ions and ligands, resulting in the complete destruction of the morphology of the MOF. The mapping images (Fig. 2(g–i)) of MIL-53(Fe : Co = 1 : 4) confirmed the presence of Fe and Co elements distributed uniformly across the surface of the material. In addition, we found that when MIL-53(Co) was prepared into a catalyst solution, the colour of MIL-53(Co) changed from a purple powder to a pink solution, as shown in the inset images. In order to observe whether the microstructure of MIL-53(Co) changes, we collected the SEM images of the powder and solution.

Shown in Fig. 3 is a comparison of the SEM images of the powder and solution of MIL-53(Co). We can clearly observe that the morphology is completely destroyed when it dissolves in isopropyl alcohol, which shows that the MIL-53(Co) was
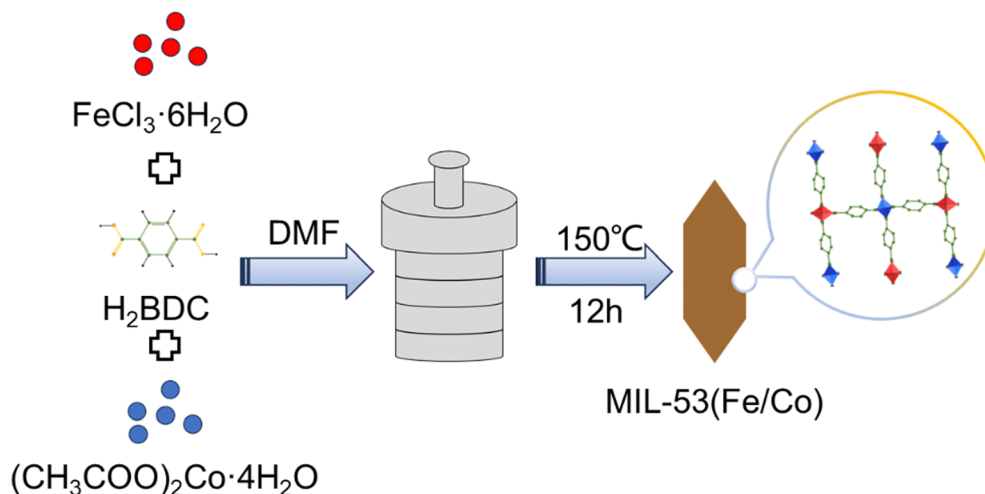

Fig. 1 Schematic representation of the synthesis of MIL-53(Fe/Co).
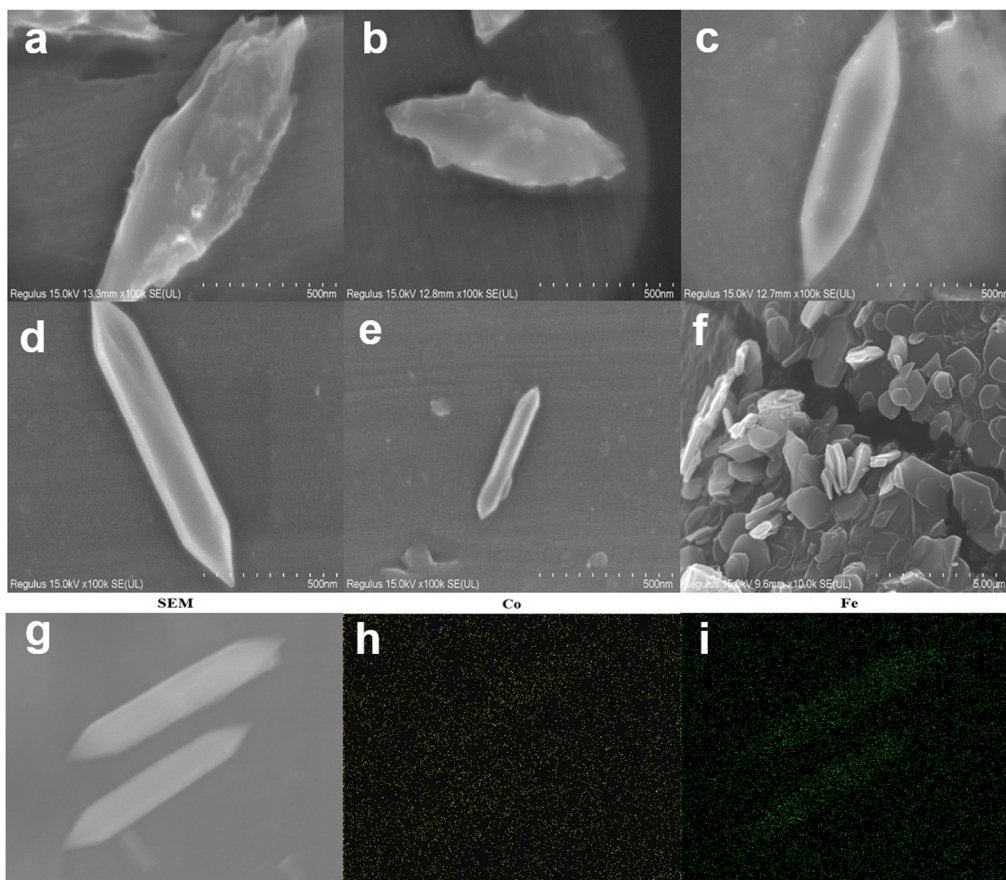
Fig. 2 SEM image of MIL-53(Fe) (a), MIL-53(Fe : Co = 4 : 1 (b), 3 : 2 (c), 2 : 3 (d), 1 : 4 (e)), MIL-53(Co) (f) and MIL-53(Fe : Co = 4 : 1), and (g) mapping of Co (h) and Fe (i).

extremely unstable and further supports the above conjecture. Therefore, we will not compare the electrocatalytic WOR performance of the MIL-53(Co) and MIL-53(Fe/Co) in the following.

To determine the crystal structure and atomic arrangement, X-ray diffraction analysis was performed on the synthesized samples. As shown in Fig. 4, the characteristic diffraction peaks of the MIL-53(Fe) material matched well with the standard XRD simulation-MIL-53(Fe) results in the reported literature,[28] indicating the high crystallinity of MIL-53(Fe).

Upon the introduction of Co into MIL-53(Fe), the diffraction peak of MIL-53(Fe) at 10.5° and 17.5° experienced a slight shift towards a lower angle (10° and 17°). This transformation can be attributed to the fact that the ionic radius of Co^{2+} (0.0745 nm) is much greater than that of Fe^{3+} (0.064 nm). When Co replaces Fe in MIL-53(Fe), the crystal plane spacing increases and lattice distortion occurs, which causes the diffraction peak to shift lower.[41] Thus, the XRD results show that MIL-53(Fe) and MIL-53(Fe/Co) were successfully synthesized. In addition, we
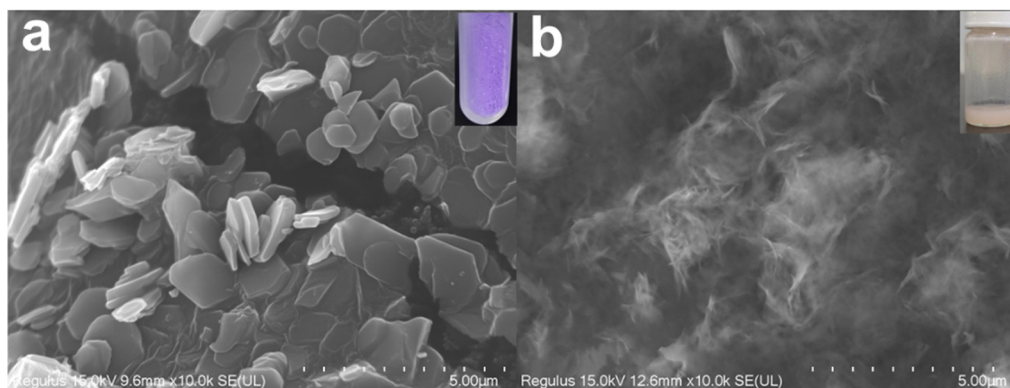

Fig. 3 SEM image of MIL-53(Co) ((a) powder, (b) solution, inset: photos of the power and solution).
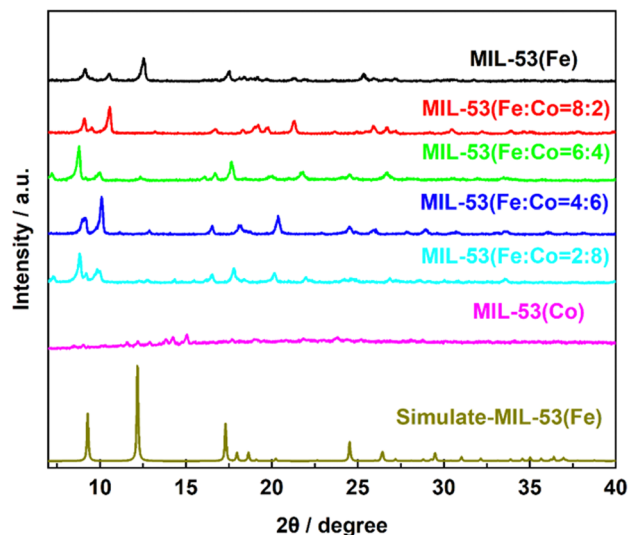
Fig. 4 XRD image of MIL-53(Fe), MIL-53(Fe/Co) and simulate-IL-53(Fe).

performed the crystal structure and atomic arrangement of MIL-53(Co) by XRD.

As shown in Fig. 4, the XRD analysis reveals that when only single-metal Co was present, the diffraction peak at $17.5°$ is almost non-existent, indicating that Co atom doping can accurately replace Fe atoms, leading to the destruction of the corresponding lattice faces. Meanwhile, the destruction of the original ordered structure of MIL-53(Fe) weakened the connection between metal ions and ligands, which caused the structure of MIL-53(Co) to be extremely unstable, supporting the previous inference.

XPS was conducted to characterize the chemical elemental composition and valence states of MIL-53(Fe/Co), MIL-53(Fe) and MIL-53(Co). The XPS survey spectrum of MIL-53(Fe/Co) confirms the presence of Fe and Co (Fig. 5a), indicating the successful incorporation of Co. In the high-resolution Fe 2p spectrum (Fig. 5a), the two peaks at 712 and 725.9 eV can be assigned to the $2p_{3/2}$ and $2p_{1/2}$ characteristic peaks of MIL-53(Fe), respectively, which indicates that Fe is present mainly in the Fe^{3+} valence state in MIL-53(Fe/Co) and MIL-53(Fe).[42] Notably, compared with MIL-53(Fe), the Fe 2p peak of MIL-53(Fe/Co) will be shifted to a higher energy level step by step as the proportion of Co atoms increases, suggesting that the lattice defects induced by Co substitution can modulate the electronic structure of the active Fe center. In the high-resolution spectrum of Co 2p in Fig. 5b, the binding energies of the $2p_{3/2}$ and $2p_{3/2}$ characteristic peaks of Co are located at 780.6 and 796.1 eV, with two satellite peaks at 785.5 and 802.6 eV, respectively, which show that the oxidation state of Co is +2 in MIL-53(Fe/Co) and MIL-53(Co).[28] In addition, the peaks of Fe 2p increased with increasing percentages of iron in the MIL-53(Fe/Co) catalysts, whereas the peak of Co 2p decreased with decreasing percentages of cobalt in the MIL-53(Fe/Co) catalysts.

3.2. Electrocatalytic performance of MIL-53(Fe/Co)

The electrocatalytic WOR performance of MIL-53(Fe/Co) was examined in 2.0 M $KHCO_3$. For comparison, MIL-53(Fe) was

also tested. Fig. 6a displays the LSV curves of MIL-53(Fe/Co) and MIL-53(Fe), respectively. The current density for MIL-53(Fe/Co) increased steadily with increased potential of the working electrode in the potential range of 1.5–2.3 V (*vs.* RHE). On comparison of MIL-53(Fe/Co) and MIL-53(Fe), the current density increased gradually with increased Co content at low overpotential and the MIL-53(Fe : Co = 1 : 4) achieved the highest current density. This was consistent with the above morphological changes, indicating that the change of MIL-53(Fe/Co) morphology improved its catalytic performance with the increase of the Co content. In addition, we calculated the overpotential of MIL-53(Fe/Co) and MIL-53(Fe), as shown in Fig. 6b. The overpotential of the bimetal-based MOF was lower than that of the single metal-based MOFs. Therefore, the MIL-53(Fe/Co) exhibited better performance of electrocatalysis water oxidation. The reason may be that the synergistic interaction between Fe/Co bimetals improves the catalytic performance of water oxidation of MIL-53(Fe/Co).

In addition, stability also plays a key role in the practical application of the catalyst, so we studied the stability of MIL-53(Fe/Co) and MIL-53(Fe). As demonstrated in Fig. 6c, MIL-53(Fe/Co) displays remarkable durability at a fixed potential of 2.03 V (*vs.* RHE) over 6 h of electrolytic water oxidation, indicating that both the MIL-53(Fe/Co) bimetallic MOF and MIL-53(Fe) monometallic MOF have good stability during electrocatalytic water oxidation.

To further understand the catalytic kinetics of the WOR process, electrochemical impedance spectroscopy (EIS) was performed. Fig. 6d shows the Nyquist plots of MIL-53(Fe/Co) and MIL-53(Fe). Clearly, the semicircle radius of MIL-53(Fe/Co) is significantly reduced, indicating excellent charge-transfer capability and excellent WOR intrinsic activity relative to MIL-53(Fe). In addition, to further investigate the charge transfer resistance, EIS was performed and the fitting circuit was inserted in Fig. 6d. The fitting equivalent circuit showed a charge transfer resistance of R_{ct} in parallel with a constant phase element CPE related to the double layer, both coupled with the electrolyte resistor R_s. We could deduce that the charge transfer resistance decreased from $3.4 \times 10^{11}\ \Omega$ to $2.2 \times 10^{4}\ \Omega$ with Co atoms replacing Fe atoms, which was consistent with the LSV data. Thus, the results above confirm the change of microstructure of MIL-53(Fe) after Co doping and the synergistic effect between Fe/Co improves the electrocatalytic performance of $2e^{-}$ WOR of the MIL-53(Fe/Co) bimetallic MOF.

To assess the changes in the material after the reaction, the surface morphology of the catalysts after the reaction was further examined by SEM (Fig. 7a). Compared with the MIL-53(Fe : Co = 1 : 4) before the reaction, there is no significant difference in the morphology of MIL-53(Fe : Co = 1 : 4) after the reaction. This indicates that the morphology is still maintained after long-term reaction. In addition, the XPS spectra (Fig. 7b) were measured to characterize the metal oxidation states. The results show that the spectra of Fe 2p and Co 2p show no changes in the MIL-53(Fe : Co = 1 : 4) before and after the reaction. Compared with the precatalyst, catalysts normally show better consistency after the reaction.[43] These above results show
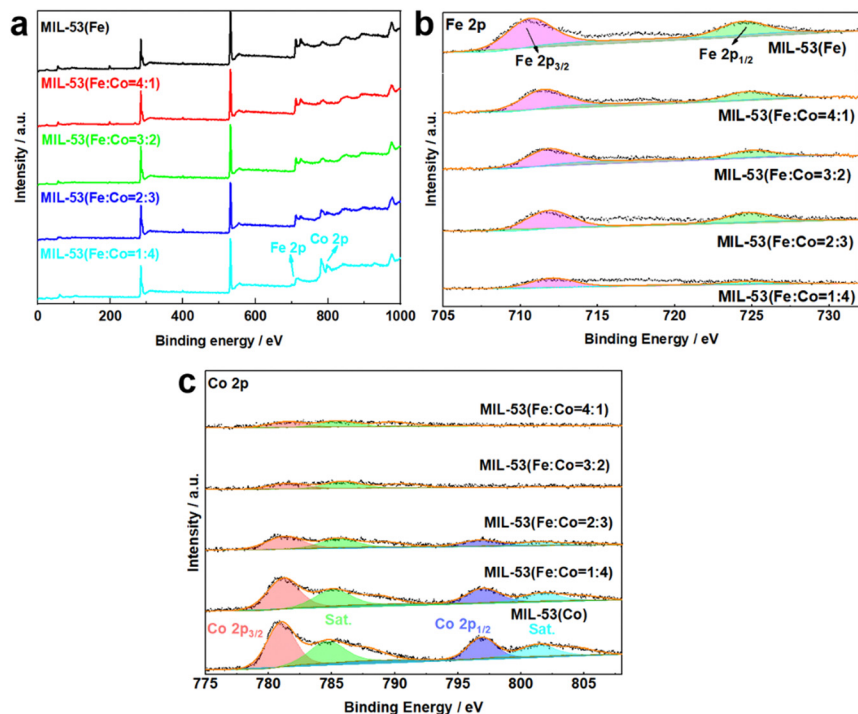
Fig. 5 XPS spectra of MIL-53(Fe) and MIL-53(Fe/Co) (a), Fe 2p (b) of MIL-53(Fe) and MIL-53(Fe/Co) and Co 2p (c) of MIL-53(Fe/Co) and MIL-53(Co).

the morphology and structure of the catalysts before and after the reaction.

In addition, the oxygen vacancies of MIL-53(Fe : Co = 1 : 4) before and after the reaction were tested by EPR in Fig. 8. There
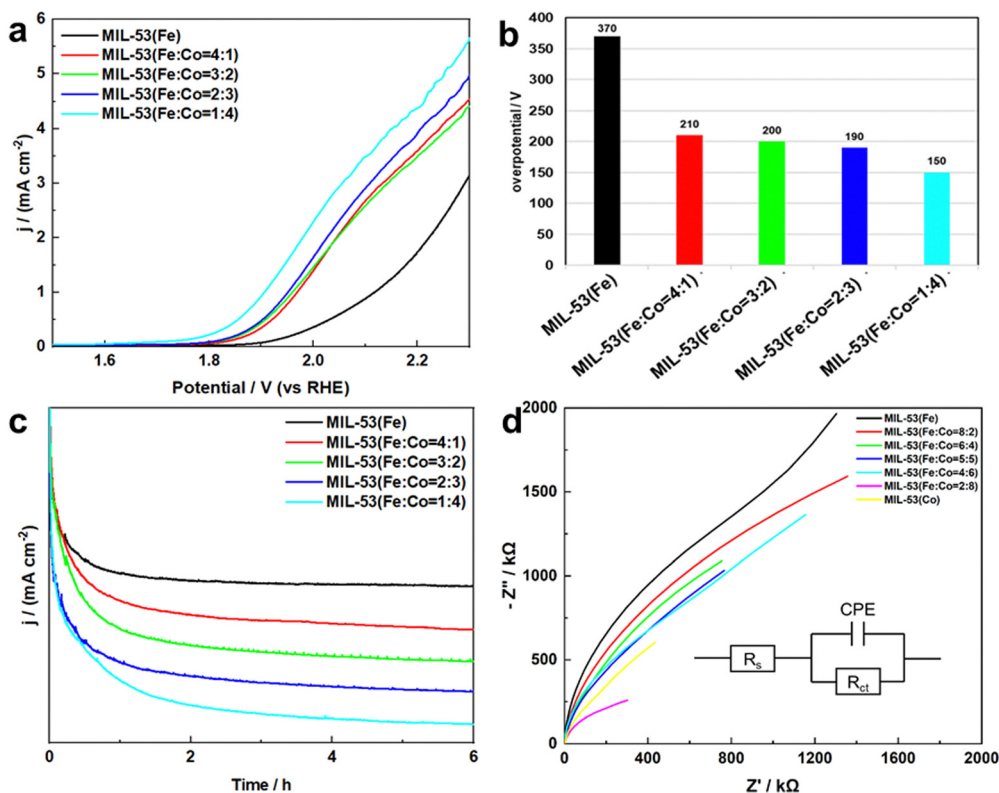

Fig. 6 (a) LSV of MIL-53(Fe) and MIL-53(Fe/Co), (b) overpotential of MIL-53(Fe) and MIL-53(Fe/Co) at 1 mA cm^{-2}, (c) stability test of MIL-53(Fe) and MIL-53(Fe/Co) and (d) EIS of MIL-53(Fe) and MIL-53(Fe/Co) (inset: Equivalent circuit model).
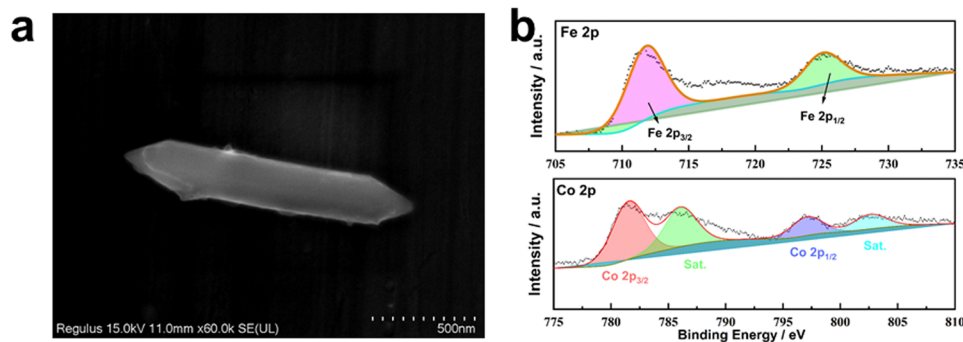
Fig. 7 SEM image (a) and XPS spectra (Fe 2p and Co 2p) (b) of MIL-53(Fe : Co = 1 : 4) after reaction.

are apparent symmetrical and sharp signals at g = 2.0043 (Fig. 8a) and g = 2.002 (Fig. 8b) in MIL-53(Fe : Co = 1 : 4) after the reaction, which are attributed to oxygen vacancies.[44] The oxygen vacancies still exist in the catalysts after the reaction but with reduced intensity, which may be the influence of electron transfer.[45]

3.3. H_2O_2 production

The cumulative H_2O_2 yield measurement of MIL-53(Fe : Co = 1 : 4) was conducted in a H-type electrolytic cell with SCE as the reference electrode, graphite rod as the counter electrode, and the MIL-53(Fe : Co = 1 : 4) supported on FTO as the working electrode. A Nafion 117 membrane was used for separating the electrolytic cells. The H_2O_2 production performances were investigated by measuring the H_2O_2 evolution rate. Firstly, the standard spectral curve of H_2O_2 was obtained using the traditional $Ce(SO_4)_2$ titration method, as shown in Fig. 9a. In addition, the H_2O_2 production of MIL-53(Fe : Co = 1 : 4) was measured using a chronoamperometry method for 60 min. The same amount of electrolyte was collected from the anode chamber at intervals of 5, 10, 20, 30, 45 and 60 minutes to detect the H_2O_2 production. Based on the standard spectral
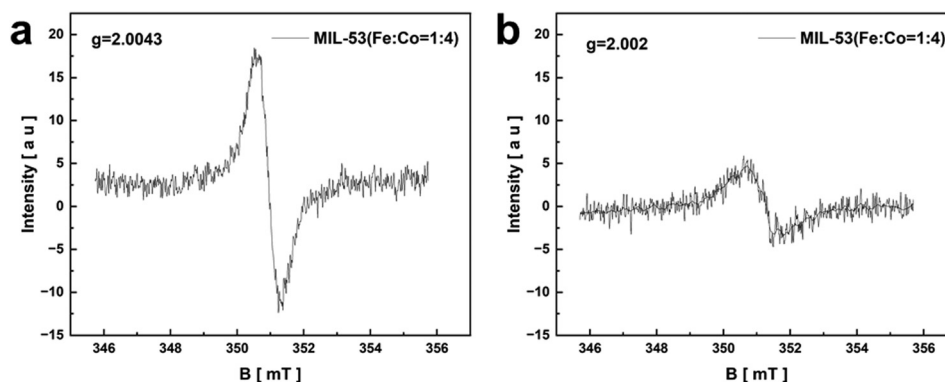

Fig. 8 EPR spectrum of MIL-53((Fe : Co = 1 : 4)) before (a) and after (b) reaction.
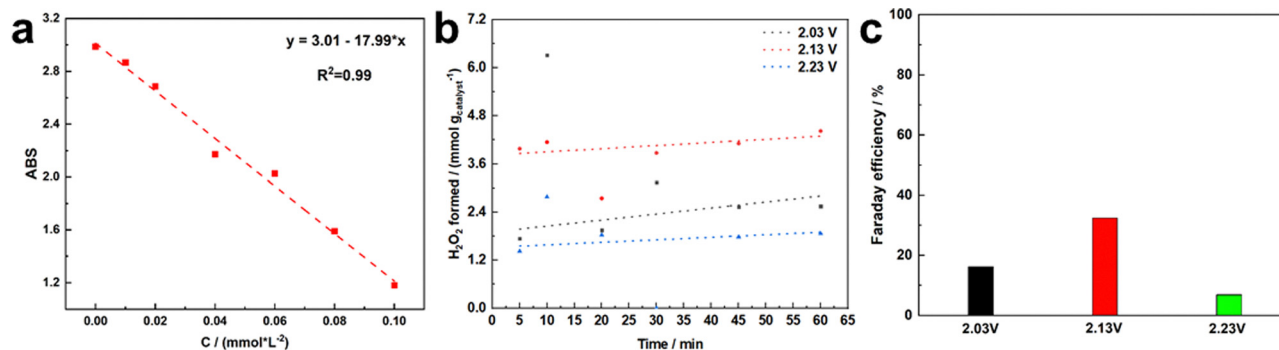

Fig. 9 Standard curve for the hydrogen peroxide test (a), time course for H_2O_2 accumulation (b) and Faraday efficiency with MIL-53(Fe : Co = 1 : 4) at different electric potentials (c).
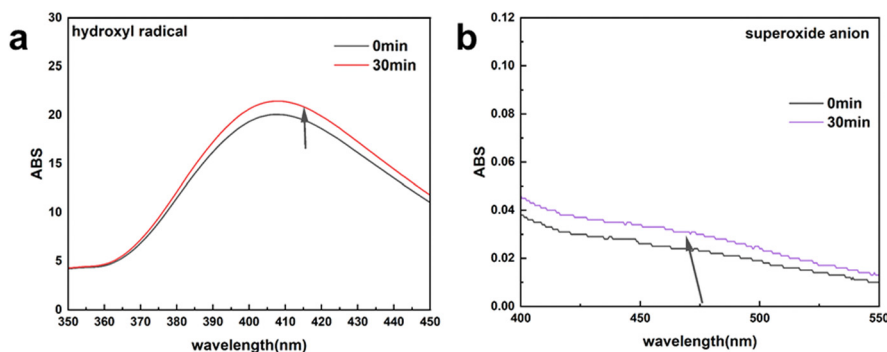
Fig. 10 Absorbance spectra of electrolyte solution-trapped hydroxyl radicals (a) and superoxide anions (b).

curve of H_2O_2, the yield of H_2O_2 was gained, as shown in Fig. 9b, and the H_2O_2 production generally showed an upward trend with time. Compared to the H_2O_2 production under different potentials (2.03 V, 2.13 V, 2.23 V *vs.* RHE), the H_2O_2 production of MIL-53(Fe : Co = 1 : 4) was the highest at 2.13 V *vs.* RHE. H_2O_2 production was achieved by MIL-53(Fe : Co = 1 : 4) with a production rate of 4 mmol/gcatalyst. In addition, we calculated the Faraday efficiency (FE) of MIL-53(Fe : Co = 1 : 4) under different potentials (Fig. 9c). The FE was also the highest at 2.13 V *vs.* RHE and reached 30%.

In addition, except for the produced H_2O_2, the hydroxyl radicals and superoxide anions were analyzed by fluorimetric assay and UV-vis spectrophotometer assay, respectively.[46] The fluorescence intensity (Fig. 10a) and UV-vis absorption peak (Fig. 10b) also displayed no significant change in the absorption peak before and after the electrocatalytic reaction. These results indicate that a small amount hydroxyl radicals and superoxide anions are generated during the production of H_2O_2. The generation of superoxide anions and hydroxyl radicals may stem from the interaction of metals in MIL-53(Fe : Co = 1 : 4) with the produced H_2O_2.[47]

4. Conclusions

To conclude, we successfully prepared a MIL-53(Fe/Co) bimetallic MOF and MIL-53(Fe) monometallic MOF by a hydrothermal method and characterized the morphology and structure. The structural characterization and elemental analysis showed that Co ions were successfully doped into MIL-53(Fe), which adjusted the morphology of MIL-53(Fe) and made it more regular. Meanwhile, we explored the electrocatalysis water oxidation properties of MIL-53(Fe/Co). The overpotential of MIL-53(Fe/Co) was only 150 mV at 1 mA cm^{-2}, which was lower than that of MIL-53(Fe). Therefore, the MIL-53(Fe/Co) exhibited good performance in electrocatalytic water oxidation. This may be attributed to the alteration of the microstructure of MIL-53(Fe) after Co ion doping and the synergistic interaction between Fe/Co bimetals. In addition, the ability of MIL-53(Fe/Co = 1 : 4) to electrocatalyse water oxidation to produce H_2O_2 at different potentials was also investigated, and it was found that MIL-53(Fe/Co = 1 : 4) had the highest H_2O_2 production at 2.13 V (*vs.* RHE).

Author contributions

Kunpeng Liu and Xu Wang: conceptualization, methodology, investigation, characterize materials, performance tests, writing – original draft. Nan Wang: conceptualization, methodology, writing – review & editing, funding acquisition. Ruiyong Zhang: resources, funding acquisition. Meinan Yang: performance tests. Baorong Hou: resources. Wolfgang Sand: funding acquisition.

Data availability

The data that support the findings of this study are available from the corresponding authors upon reasonable request.

Conflicts of interest

The authors declare no conflict of interest.

Acknowledgements

Notes and references

1 A. Herman, J. L. Mathias and R. Neumann, *ACS Catal.*, 2022, **12**, 4149–4155.
2 S. Mavrikis, S. C. Perry, P. K. Leung, L. Wang and C. P. de León, *ACS Sustainable Chem. Eng.*, 2021, **9**, 76–91.
3 L. J. Li, Z. F. Hu and J. C. Yu, *Angew. Chem., Int. Ed.*, 2020, **59**, 20538–20544.
4 C. Ling, A. P. Liang, C. L. Li and W. H. Wang, *J. Zhejiang Univ., Sci., A*, 2023, **24**, 377–386.
5 X. J. Shi, S. Back, T. M. Gill, S. Siahrostami and X. L. Zheng, *Chem*, 2021, **7**, 38–63.
6 Y. Yao, H. Wang, K. Dong, H. Li, J. Liang, R. Li, S. Sun, Z. Cai, X. He, D. Zheng, Y. Luo, S. Alfaifi, D. Ma, W. Hu and X. Sun, *J. Mater. Chem. A*, 2023, **11**, 22154–22160.

7 Z. Deng, L. Li, Y. Ren, C. Ma, J. Liang, K. Dong, Q. Liu, Y. Luo, T. Li, B. Tang, Y. Liu, S. Gao, A. M. Asiri, S. Yan and X. Sun, *Nano Res.*, 2022, **15**, 3880–3885.

8 K. Dong, J. Liang, Y. Wang, Z. Xu, Q. Liu, Y. Luo, T. Li, L. Li, X. Shi, A. M. Asiri, Q. Li, D. Ma and X. Sun, *Angew. Chem., Int. Ed.*, 2021, **60**, 10583–10587.

9 W. L. Guo, S. S. Wang, Y. Q. Xie, C. Fang, L. L. Liu, Q. Lou, X. Lian and G. Henkelman, *ACS Sustainable Chem. Eng.*, 2023, **11**, 12114–12122.

10 Y. H. Jiang, L. L. Guan, Y. J. Jiao, C. X. Yu, F. Zhao, X. W. Zhou and Z. Liu, *Electron. Mater. Lett.*, 2024, **20**, 199–206.

11 J. H. Wang, D. Kim, J. H. Park, S. Ryu, M. Shokouhimehr and H. W. Jang, *Energy Fuels*, 2023, **37**, 17629–17651.

12 J. Baek, Q. Jin, N. S. Johnson, Y. Jiang, R. Ning, A. Mehta, S. Siahrostami and X. L. Zheng, *Nat. Commun.*, 2022, **13**, 7256.

13 S. R. Kelly, X. J. Shi, S. Back, L. Vallez, S. Y. Park, S. Siahrostami, X. L. Zheng and J. K. Norskov, *ACS Catal.*, 2019, **9**, 4593–4599.

14 X. J. Shi, S. Siahrostami, G. L. Li, Y. R. Zhang, P. Chakthranont, F. Studt, T. F. Jaramillo, X. L. Zheng and J. K. Norskov, *Nat. Commun.*, 2017, **8**, 701.

15 W. Guo, Y. Xie, S. Tang, B. Yu, X. Lian, G. Henkelman and X. Liu, *Appl. Surf. Sci.*, 2022, **596**, 153634.

16 S. G. Xue, L. Tang, Y. K. Tang, C. X. Li, M. L. Li, J. J. Zhou, W. Chen, F. Zhu and J. Jiang, *ACS Appl. Mater. Interfaces*, 2020, **12**, 4423–4431.

17 A. Nadar, S. S. Gupta, Y. Kar, S. Shetty, A. P. van Bavel and D. Khushalani, *J. Phys. Chem. C*, 2020, **124**, 4152–4161.

18 C. Q. Zhang, R. H. Lu, C. Liu, L. Yuan, J. Wang, Y. Zhao and C. Z. Yu, *Adv. Funct. Mater.*, 2021, **31**, 2100099.

19 C. Q. Zhang, J. Y. Lu, C. Liu, Y. Y. Zou, L. Yuan, J. Wang and C. Z. Yu, *Environ. Res.*, 2022, **206**, 112290.

20 D. Pangotra, L. I. Csepei, A. Roth, C. P. de León, V. Sieber and L. Vieira, *Appl. Catal., B*, 2022, **303**, 120848.

21 S. Mavrikis, M. Göltz, S. C. Perry, F. Bogdan, P. K. Leung, S. Rosiwal, L. Wang and C. P. de León, *ACS Energy Lett.*, 2021, **6**, 2369–2377.

22 C. Xia, S. Back, S. Ringe, K. Jiang, F. H. Chen, X. M. Sun, S. Siahrostami, K. R. Chan and H. T. Wang, *Nat. Catal.*, 2020, **3**, 125–134.

23 Y. Kondo, Y. Kuwahara, K. Mori and H. Yamashita, *Chem*, 2022, **8**, 2924–2938.

24 L. Chen, L. Wang, Y. Y. Wan, Y. Zhang, Z. M. Qi, X. J. Wu and H. X. Xu, *Adv. Mater.*, 2020, **32**, 1904433.

25 Z. B. Wang, H. B. Wang, P. Wang, X. W. Liu, X. F. Lei, R. Guo, J. H. You and H. Z. Zhang, *Coord. Chem. Rev.*, 2024, **499**, 215506.

26 A. Goswami, D. Ghosh, V. V. Chernyshev, A. Dey, D. Pradhan and K. Biradha, *ACS Appl. Mater. Interfaces*, 2020, **12**, 33679–33689.

27 H. Chen, Y. Liu, T. Cai, W. Dong, L. Tang, X. Xia, L. Wang and T. Li, *ACS Appl. Mater. Interfaces*, 2019, **11**, 28791–28800.

28 D. Wen, Y. Ma, G. M. Mu, Q. P. Huang, X. F. Luo, D. M. Lin, C. G. Xu, F. Y. Xie, G. Z. Wang and W. H. Guo, *Dalton Trans.*, 2023, **52**, 10662–10671.

29 B. Cui, C. Wang, S. Huang, L. He, S. Zhang, Z. Zhang and M. Du, *J. Colloid Interface Sci.*, 2020, **578**, 10–23.

30 T. Qiu, Z. Liang, W. Guo, H. Tabassum, S. Gao and R. Zou, *ACS Energy Lett.*, 2020, **5**, 520–532.

31 D. Chen, Q. Sun, C. Han, Y. Guo, Q. Huang, W. A. Goddard and J. Qian, *J. Mater. Chem. A*, 2022, **10**, 16007–16015.

32 X. Wang, Z. Qin, J. Qian, L. Chen and K. Shen, *ACS Catal.*, 2023, **13**, 10672–10682.

33 Z. Q. Li, R. Gao, M. Feng, Y. P. Deng, D. J. Xiao, Y. Zheng, Z. Zhao, D. Luo, Y. L. Liu, Z. Zhang, D. D. Wang, Q. Li, H. B. Li, X. Wang and Z. W. Chen, *Adv. Energy Mater.*, 2021, **11**, 2003291.

34 Y. Zhou, R. Abazari, J. Chen, M. Tahir, A. Kumar, R. R. Ikreedeegh, E. Rani, H. Singh and A. M. Kirillov, *Coord. Chem. Rev.*, 2022, **451**, 214264.

35 K. Dong, J. Liang, Y. Wang, L. Zhang, Z. Xu, S. Sun, Y. Luo, T. Li, Q. Liu, N. Li, B. Tang, A. A. Alshehri, Q. Li, D. Ma and X. Sun, *ACS Catal.*, 2022, **12**, 6092–6099.

36 M. Fan, J. Yan, Q. Cui, R. Shang, Q. Zuo, L. Gong and W. Zhang, *Molecules*, 2023, **28**, 3622.

37 J. Luo, X. Luo, Y. Gan, X. Xu, B. Xu, Z. Liu, C. Ding, Y. Cui and C. Sun, *Nanomaterials*, 2023, **13**, 2194.

38 S. Xu, H. Ni, X. Zhang, C. Han and J. Qian, *Inorg. Chem.*, 2023, **62**, 14757–14763.

39 C. H. Zhang, L. H. Ai and J. Jiang, *J. Mater. Chem. A*, 2015, **3**, 3074–3081.

40 K. Jiang, M. Luo, Z. X. Liu, M. Peng, D. C. Chen, Y. R. Lu, T. S. Chan, F. M. F. de Groot and Y. W. Tan, *Nat. Commun.*, 2021, **12**, 1687.

41 S. F. Zhang, Z. Y. Huang, T. T. Isimjan, D. D. Cai and X. L. Yang, *Appl. Catal., B*, 2024, **343**, 123448.

42 M. W. Xie, Y. Ma, D. M. Lin, C. G. Xu, F. Y. Xie and W. Zeng, *Nanoscale*, 2020, **12**, 67–71.

43 W. Zheng and L. Y. S. Lee, *ACS Energy Lett.*, 2021, **6**, 2838–2843.

44 J. Tong, J. Wang, X. Shen, H. Zhang, Y. Wang, Q. Fang and L. Chen, *Inorg. Chem.*, 2021, **60**, 10715–10721.

45 K. Dong, J. Liang, Y. Wang, Y. Ren, Z. Xu, H. Zhou, L. Li, Q. Liu, Y. Luo, T. Li, A. M. Asiri, Q. Li, D. Ma and X. Sun, *Chem. Catal.*, 2021, **1**, 1437–1448.

46 N. Wang, S. Ma, J. Duan, X. Zhai, F. Guan, X. Wang and B. Hou, *Electrochim. Acta*, 2020, **340**, 135880.

47 K. Dong, Y. Yao, H. Li, H. Li, S. Sun, X. He, Y. Wang, Y. Luo, D. Zheng, Q. Liu, Q. Li, D. Ma, X. Sun and B. Tang, *Nat. Synth.*, 2024, **3**, 763–773.